Materials & Design 236 (2023) 112502

Contents lists available at ScienceDirect

Materials & Design

journal homepage: www.elsevier.com/locate/matdes

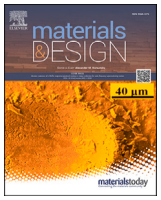

Simulation of two nanoparticle melting to understand the conductivity drop of 3D-printed silver nanowires ☆

Teja Kuruganti [a], Pooran K. Joshi [b], Monojoy Goswami [c,*]

[a] Computer Science and Engineering Division, Oak Ridge National Laboratory, 37922, Oak Ridge, TN, USA
[b] Energy Science and Technology Division, Oak Ridge National Laboratory, 37922, Oak Ridge, TN, USA
[c] Chemical Sciences Division, Oak Ridge National Laboratory, 37922, Oak Ridge, TN, USA

ARTICLE INFO

Keywords:
Printed electronics
Nanoparticle sintering
Molecular dynamics simulations
Silver conductivity

ABSTRACT

The future flexible sensor technology will require low-temperature, fast processing 3D printing techniques that will rely heavily on the quality of nanoparticle (NP) Ink. Electrical conductivity has been found to decrease in majority of the 3D printed electronic wires. Herein we report a fundamental understanding in drop of electrical conductivity in processed silver (Ag) line wire, generally found in Ag-nanoparticle Ink, using large-scale atomistic molecular dynamics (MD) simulations of sintering of five different sizes of Ag NPs. To preserve the high conductivity of pure silver wires, the integrity of the pristine face-centered cubic (FCC) crystalline structure must be retained in the processed line wires. Simulations show that the pristine Ag FCC structures of the nanoparticles are not recovered after melting and resolidification, instead, the resolidified material is paracrystaline. The breakdown of pristine FCC structures might be the cause of the drop in conductivity of processed Ag wires. Simulation results suggest that the intermediate size nanoparticles retain highest percentage of the pristine silver face-centered cubic (FCC) structure after pulse treatments. Our results show that the most promising Ag-Ink should contain smaller to medium size silver NPs that can retain FCC structure after 3D printing of the Ag-Ink.

1. Introduction

In recent years, additively manufactured materials have been extensively investigated to meet the fast-paced manufacturing demands of materials with enhanced functionality for the application in flexible printed electronics, sensors etc [1–4]. The range of materials that can be directly processed using additive manufacturing (3D printing) is growing rapidly, especially in polymers and biopolymers, ceramics, nanoparticles, organic and inorganic semiconductors and various different dielectric materials [5,6]. One of the major requirements in flexible electronic applications is the ability to fabricate electronic devices on flexible substrates at a low-cost with fast 3D printing processibility without compromising the basic electronic properties of the fabricated electronic devices [7,4]. In particular, in flexible sensor applications, a large number of flexible electronic can be additively manufactured at a low-cost and high fabrication rate. Low-temperature processing of contact free, inkjet-based printed electronics for environmental sensors employing pulse-thermal processing (PTP) has been recently used to develop flexible sensors on plastics, paper and fabric substrates [8–12]. Extensive efforts are underway to process diverse range of materials on flexible substrates employing single wavelength lasers or broadband lamps for sintering of metal particles using Inkjet printing technology [13–15]. Modeling and direct-write printing study focuses on photonic sintering kinetics of printed metal lines on a sub-second processing time range [3]. Broadband photonic sintering is suitable for metal contact and interconnect processing on low-temperature flexible substrates for printed electronic applications [16,17].

* Corresponding author.
E-mail addresses: kurugantipv@ornl.gov (T. Kuruganti), goswamim@ornl.gov (M. Goswami).

https://doi.org/10.1016/j.matdes.2023.112502
Received 7 September 2023; Received in revised form 6 November 2023; Accepted 14 November 2023
Available online 20 November 2023

Sintering is critical to fuse nanoparticles to obtain the required bulk properties, in this case, conductivity for real-time electronic applications when the electronics are designed using 3D printed technologies. Sintering is a two step process, (1) spontaneous coalescence of nanoparticle (NP), and (2) Ostwald ripening. This two-step sintering process is driven by the surface-to-volume energy the nanoparticles of the order of 10 to 100 nanometers (nm) [18]. Detailed study of silver (Ag) NP size-dependence on these two-step processes are elucidated by Tang et al. [16]. It is possible to achieve high electrical conductivity in sintered silver (Ag) metal lines with photonic pulse width control in the range of 20 microsecond (μs) to 10 milliseconds (ms). In additional to peak pulse power in pulse processing, both the pulse-width and number of pulses have a strong influence on the electrical conductivity of the sintered metal lines [19]. Fundamental understanding of the sintering kinetics in close collaboration with the experiential evaluation will enable co-integration of diverse metal, semiconductor, and insulators to realize multi-layer active/passive electronic devices. Such an understanding is critical to exploit rapid photonic processing techniques to bring high performance materials on flexible platform where the substrate damage defines the integration possibilities [20]. The combination of computer simulation, and ultrafast photonic processing demonstrate a path towards high throughput processing of nanoscale materials in a roll-to-roll manufacturing environment.

However, due to the apparent changes of intrinsic functionality of metals during sintering processes, challenges remain in designing printed electronic materials for electronic applications and sensing that require high precision synthesis preserving the fundamental atomistic properties of the pristine metal [21,22]. There have been several molecular dynamics studies to understand nanoparticle melting and sintering behaviors for different metals. Wu et al. [23] have shown that smaller copper (Cu) NPs melt at lower temperature than bulk melting temperatures resulting in smaller Cu nanoparticles bonding temperature which is desirable for application. Moreover, their work has also shown that the sintering process forms a neck area that alters Cu-Cu bonding and hence the pristine lattice structure of Cu NPs. In aluminium and Cu nanoparticle sintering processes, Abedini et al. [24] have shown that there is a strong correlation between crystalline structure and sintered NP sizes and processing temperatures. In our previous experimental work we observed that the printed wires show higher resistivity therefore lower conductivity than pristine face-centered-cubic (FCC) Ag while using pulse thermal processing to design flexible sensors from Inkjet printed Ag metals [8]. The pristine Ag resistivity and conductivity at 20^oC are $1.59 \times 10^{-8}\Omega.m$ and $6.3 \times 10^7 Simens/m$ respectively.

In the present study, we focus on obtaining fundamental physics understanding of the stability of pristine FCC structure of Ag NPs before and after sintering. It is important to note that the pristine FCC structure with 4.09Å lattice constant provides the highest electrical conductivity of Ag. While the electrical conductivity of metal is a quantum phenomena explained by band theory, classically the pristine FCC structure of Ag is key to achieving the highest conductivity of Ag out of all metal. We hypothesize that the drop in the conductivity (or increase in resistivity) is a result of breakdown of the pristine FCC structure of Ag NPs in the Ag-Ink used for InkJet printing process. To support our hypothesis, we perform MD simulations of sintering of two NPs of different sizes and analyze the crystallinity of fused Ag nanoparticles after sintering to determine the Ag lattice structure. Once the structure is determined, we compare the structure with pristine FCC Ag lattice to examine the reason behind breakdown of the FCC structure. The article is arranged in the following manner, we describe the simulation methods in detail followed by a results and conclusion sections.

2. Molecular dynamics simulation method

Atomistic MD simulations are carried out for five different sizes of nanoparticles (NP). Two NPs of diameter 10 nm, 20 nm, 30 nm, 40 nm and 50 nm are placed next to each other in a box of variable dimensions (See SI figure Fig. S1). The nanoparticles are build from the Ag crystallographic structure, lattice constant, 4.09Å. Five different sizes two nanoparticle systems consist of 57,794 (10 nm), 524,134 (20 nm), 1,694,594 (30 nm), 3,941,562 (40 nm), and 7,605,502 (50 nm) number of atoms respectively. The number of atoms shows the simulating system becomes huge for 50 nm Ag particles. To test how big system we could simulate at Summit supercomputer and also get closer to the experimental Ag-Ink nanoparticle size, we have simulated a trial system of 100 nm (1 μ) nanoparticle consisting of 60,564,030 atoms. We successfully perform the melting simulation of 100 nm particles that will be presented at the end of the results. The results will be discussed based on the 10 nm to 50 nm particle size systems without altering the pristine FCC structure of Ag before, during and after pulse treatments. Because the focus of this work to understand the fundamental classical explanation of the decrease of conductivity in Ag nanowires, a smaller NP suffices the purpose. Similarly, we need to adjust a few of the experimental parameters due to the length- and time-scale constraints that is inherent to large-scale computer simulations. Due to these limitations, we scaled the pulse power and durations to enable tractable simulations. In place of standard pulse used experimentally, 1.3 J/cm^2 for 500 μs [10,9], we increase the pulse energy and decrease the pulse-time to obtain fully melted two Ag nanoparticle. This adjustment of pulse sizes led to 30 eV/ps pulse for 1.0 ns for 10 nm Ag particles sintering. The pulse width increases as a function of radius cubed (volume) for larger Ag nanoparticles due to the spherical nature of the particles. All of these simulations are carried out at Oak Ridge Leadership Computing Facility (OLCF), Summit supercomputer and Cori supercomputer at National Energy Research Scientific Computing Center (NERSC).

The interatomic interactions (energies) are obtained multibody embedded atom model (EAM) potential [25] given by,

$$E_i = F_\alpha\left(\sum_{j\neq i}\rho_\beta r(ij)\right) + \frac{1}{2}\sum_{j\neq i}\phi_{\alpha\beta}(r(ij)$$

where $r(ij)$ is the distance between i and j atoms, $\phi_{\alpha\beta}$ is a pair-wise potential, ρ_β is the electron density from one atom of type β at the location of another atom and F_α is the embedding function representing energy needed to insert α-type i atom in the electron cloud. Both the terms of the above equation sums over all the atoms within the cutoff distance. The cutoff distance is obtained from the tabulated value of the EAM potential in DYNAMO-style data format. The EAM force-field parameters are obtained from the seminal works of Foiles et al. [26]. The minimization of the NPs is performed at $275K$. Thereafter, all of these NP temperatures are raised to 60^oC within a nanosecond and the NPs are equilibrated for another 1 ns. Thereafter, pulses of different width for different Ag NP sizes are used to fuse (melt) the Ag NPs together. The pulses are introduced for 1 ns and then equilibrated at higher temperatures for 1 ns more. The cooling down of the high temperature equilibrated structures to 27^oC are done in two steps of 1 ns each. The 27^oC cooled down fused line structures are then compared with the initial Ag NP structures. As discussed before, the time- and length-scales of the simulations are different from the experiments due to computational constraints of smaller length and time-scales in computer models. The largest simulation contains > 7.6 million Ag atoms for 50 nm particles, except for the trial run for 100 nm particles. To our knowledge, this is the largest simulation to date on Ag NP sintering. All the simulations are performed using Large-scale Atomic/Molecular Massively Parallel Simulator (LAMMPS) molecular dynamics package [27].

3. Results and discussion

Large-scale MD simulations are performed on a pair of 10, 20, 30, 40, and 50 nm particles. Once equilibrations for each of the systems are achieved, we have collected the statistics to understand the structure and dynamics of the sintered nanoparticles. The snapshots and calculations percentage of crystal structures are carried out using Ovito [28]

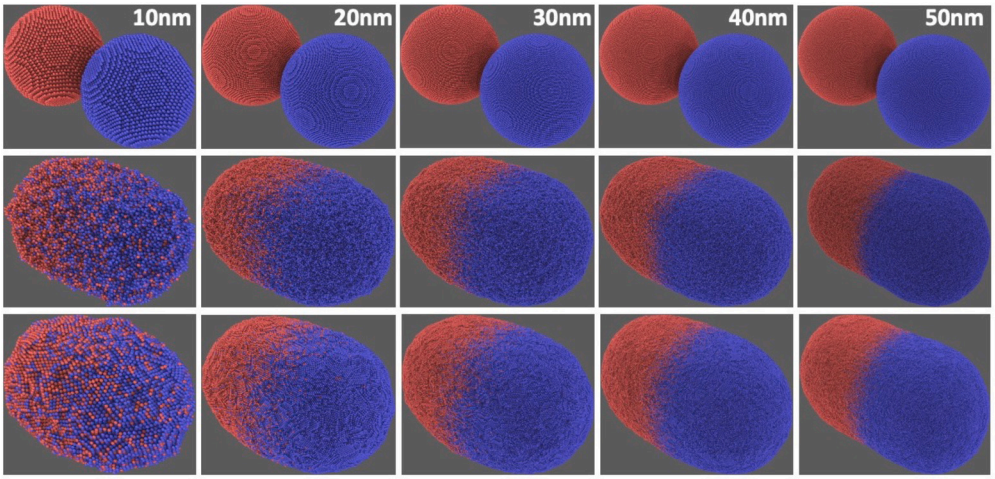

Fig. 1. Simulation snapshots of two silver nanoparticle at different phases before, during and after sintering using heat pulse. Top panel, equilibrated structure before the application of pulse. Middle panel, after applying the pulse. Bottom panel, equilibrated structures after cooling down to 27^{o}C. Left to right, the columns reflect 10 nm, 20 nm, 30 nm, 40 nm and 50 nm particle sintering. The red and blue colors of the NPs are used to distinguish between two nanoparticles, however, both are Ag nanoparticle of same size.

software and radial distribution function (RDF) calculations were performed using VMD software.

In Fig. 1, we show the simulation snapshots before, during and after the applied external pulse for 10 nm to 50 nm Ag NPs. The different NP sizes are shown along the columns in Fig. 1. The top represents the equilibrated Ag NPs before pulse application. The middle panel of Fig. 1 shows the Ag NPs melted together to form a line wire structure after sintering with pulse and equilibrating at above melting temperature. The individual NP structures are colored red and blue to distinguish individual NPs during melt and line-wire formation. During melting, atoms from the individual NPs can be seen well dispersed at the interface within different NP domains. A distinctly similar structural pattern has been observed in mechanical sintering of nanoparticles to form NP superlattices by Li et al. [29]. The bottom panel shows the structures after cooling down to 27^{o}C. Once melted the FCC structures of pristine Ag break down completely (middle panel of Fig. 1). After cooling to 27^{o}C (bottom panel), the final structures exhibit reemergence of crystalline domains, but lack the pristine FCC structure of Ag. The atomistic details of these structures will be obtained from the radial distribution function (RDF) analysis later in this section.

Joining during sintering processes occurs by migration of atoms primarily along the interfaces. Thus, the surface energy and curvature of spherical NPs become the dominant factors in joining during sintering processes. Therefore, the phase transition (due to melting) temperature during sintering can be quantified by the change in potential energy as temperature increases [30]. In Fig. 2a-e, we show the potential energy versus temperature relationship curve for 10 nm to 50 nm NPs. The phase transformation of the NPs can be observed by a sudden jump in potential energy around the melting temperature, T_m, due to a large amount of energy absorbed by the NPs to go from solid to liquid state. The melting temperatures are obtained from the peak position of the first derivatives of the potential energy versus temperature curves for 10 nm to 50 nm (Fig. 2a-e). The peak positions of the first derivatives in Fig. 2f show right shift in the temperature scale indicating an increase in T_m as NP size increases. Melting temperature as a function of NP sizes is shown in Fig. 2g. In Fig. 2h the melting temperature, T_m, is tabulated for different NP sizes that varies from 1116.37 K to 1260.66 K from 10 nm to 50 nm Ag NPs. Bulk silver melting temperature is 961.8^{o}C, i.e., 1234.95 K. From the tabulated values of the T_m (Fig. 2h), it can be seen that bulk melting is already achieved at 40 nm Ag particle size within 0.44% of bulk T_m. From Fig. 2(g) and Table 2(h), it can be seen that the melting temperature decreases with the decrease in NP sizes. The well-established Gibbs-Thomson model [31] (GT-model) relates the nanoparticle radius with the melting temperature of the nanoparticles, and is given by

$$T_m^{\mathrm{NP}} = T_m^{\mathrm{Bulk}} - \frac{\left[2\left(T_m^{\mathrm{Bulk}} + 273.15\right)\sigma_{sl}\right]}{\Delta H_f^{\mathrm{Bulk}}\rho_s r}$$

Where T_m^{Bulk} is the bulk Ag melting temperature, σ_{sl} is the solid-liquid interfacial energy of the Ag, $\Delta H_f^{\mathrm{Bulk}}$ is the latent heat of melting of bulk material and ρ_s is the density of material in its solid state and 'r' is the NP radius. Simplifying the GT-model to fit the NP sizes versus T_m data in Fig. 2(g), the fitting function of the above equation becomes, $f(r) = A - B/r$, where $A = T_m^{\mathrm{Bulk}}$ is the Ag bulk melting temperature, and $B = \left[2\left(T_m^{\mathrm{Bulk}} + 273.15\right)\sigma_{sl}\right] / \Delta H_f^{\mathrm{Bulk}}\rho_s$. Fitting the Fig. 2(g) curve gives $T_m^{\mathrm{Bulk}} = 1273.3K$, which is within 3% Ag bulk melting point, $1234.95K$. Therefore, the calculations for nanoparticle melting temperature satisfy the full melting properties Ag metal.

Furthermore, for 50 nm Ag NPs, the bulk temperature is 1260.66 K, 2.1% higher than bulk T_m, which is significantly higher than the T_m for a 50 nm particle. In the case of sintering, the sintering temperature (T_s) is different than melting temperature, and the sintering process is controlled by T_s and the total time required for sintering. The two temperatures are related by $T_s = \alpha T_m$, where the factor α is a function of the material geometry and other environmental conditions [32]. For NPs, the α values range from 0.1 to 0.3 [33,34]. Moreover, the bulk melting temperature (T_{mb}) is higher than the melting temperature, T_m, of NPs as melting temperature is suppressed during sintering processes according to modified Debye model for size dependence of melting point [35,36]. Here we observed an increase in melting temperature and α values for 40 nm and 50 nm NPs. We attribute to this to the decrease in the driving force [37] at the interface of joining of two nanoparticles in contact as smaller pulse width used in the simulations due to computational constraints.

The radial distribution function (RDF) of pristine Ag NPs before, after melting, and after processing to Ag wires are shown in Fig. 3(a)-(c). Pair correlation function or radial distribution function (RDF) is ubiquitously used in determining the detailed structure of particulate systems. The RDF, $g(r)$ is defined as,

$$g(r) = \frac{V}{N^2}\sum_{i=1}\sum_{j\neq i} < \delta(r - r_{ij}) >$$

where N is the total number of atoms and V is the volume. The RDF gives the probability of finding a pair of atoms at a distance r apart relative to the probability that can be expected from a completely random

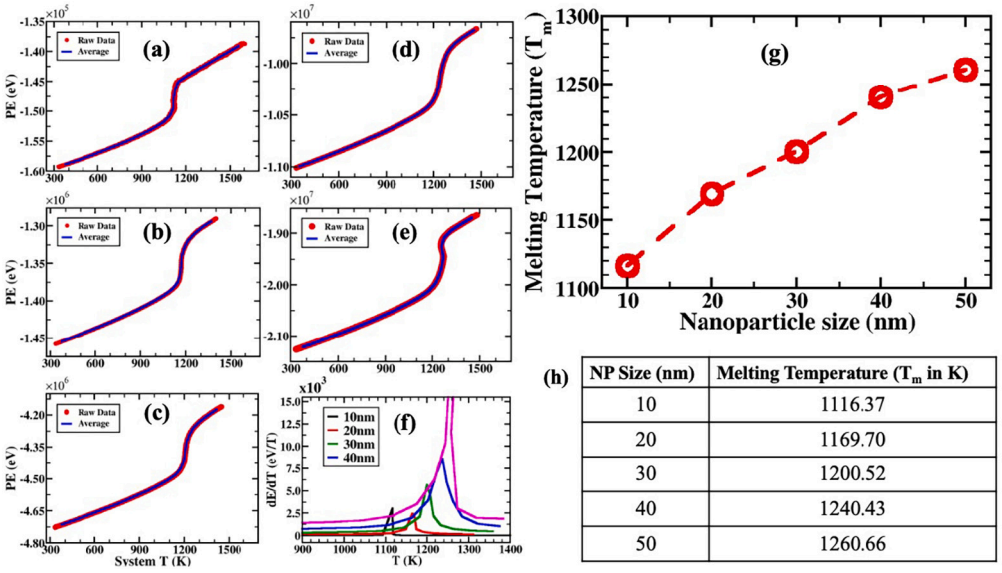

(h)

NP Size (nm)	Melting Temperature (T_m in K)
10	1116.37
20	1169.70
30	1200.52
40	1240.43
50	1260.66

Fig. 2. Melting curves of two NPs during pulse sintering. (a)-(e) Potential energy versus temperature during melting for 10 nm, 20 nm, 30 nm, 40 nm, and 50 nm. Red colors are raw data, and the blue curves through the red raw data are the running average of the raw data. (f) Calculation of melting point by taking derivative of (a)-(e) curves. Color schemes are shown in legends. (g) Melting temperature obtained from (f) plotted as a function NP sizes. The dashed red line is the guide to the eye only. (h) Tabulated values of melting temperature for different NP sizes.

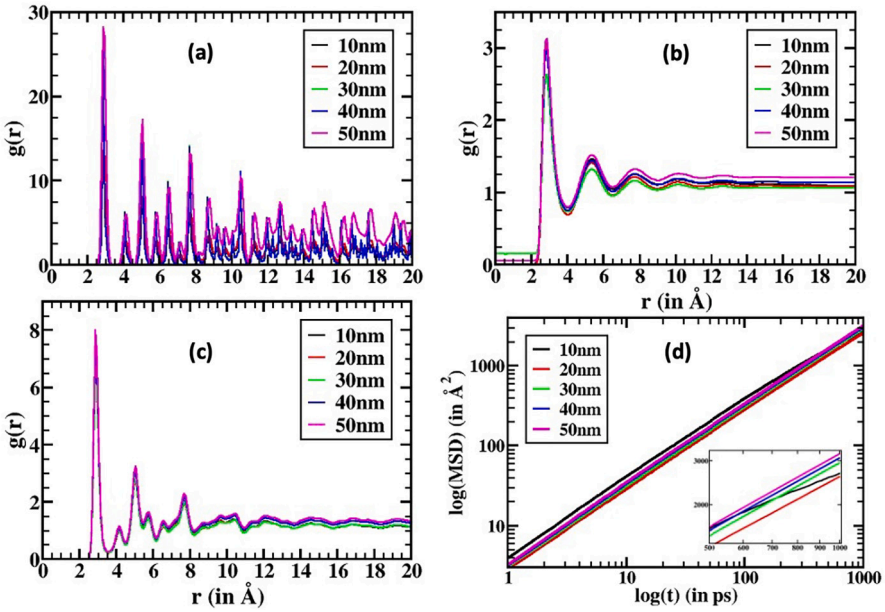

Fig. 3. Atomistic details of the NP sintering as represented by radial distribution function (RDF). (a) RDF for all the NPs before sintering. (b) RDF after pulse application showing liquid-like structures. (c) Equilibrated RDF after cooling to 27^{o}C. (d) Mean square displacement (MSD) for the Ag atoms in melt state. Inset showing the long-range MSD values representative of distinctive features at long times.

distribution of atoms at the same density. The RDFs in Fig. 3 shows structural feature for a wide range of interatomic distances. We plotted the RDF until a distance of 20Å as the melted and cooled Ag nanowires do not exhibit structural deviations beyond that length-scale. All the peaks in Fig. 3(a) RDF can be attributed to the atomic positions in the FCC lattice, i.e., the FCC crystal structure of Ag [38]. The interatomic distance, i.e., the first peak position, 2.85Å agrees well with the silver interatomic distance. Once melted, the FCC crystal forms liquid-like structure as shown in Fig. 3(b). Fig. 3(b) is plotted after one nanosecond equilibration of the sintered Ag NPs in liquid state. For all the systems, the melting exhibits liquid silver structural characteristics as was observed by Wagner *et al.* [39] in an earlier work. The cooled down structures are shown in Fig. 3(c) for all the NPs in equilibrium, exhibiting breakdown of pure crystalline Ag structure (different from Fig. 3a). As stated earlier, pristine FCC structure of the Ag is classically the major factor of Ag having the highest conductivity of all metals. As observed in Fig. 3, the breakdown of FCC structure occurs after cooling of two sintered Ag nanoparticle, hence, the sintered Ag NPs show lower conductivity as observed in experiments. The mean-square-displacement (MSD) defined by, $\text{MSD} = \frac{1}{N}\sum_{i=1}^{N}|r_i(t) - r_i(0)|^2$, at the liquid phase is plotted in Fig. 3(d). The MSD illustrates the atomic motion in liquid phase and it scales with time as $ln(\text{MSD})\ t^{\alpha}$. For a system with random motion in liquid state, $\alpha = 1.0$ at longer time-scales representing purely diffusive motion. In Fig. 3(b), the long time MSD scaling coefficient, $\alpha = 0.98$, representing purely liquid phase correlates well with the liquid structures in Fig. 3(b).

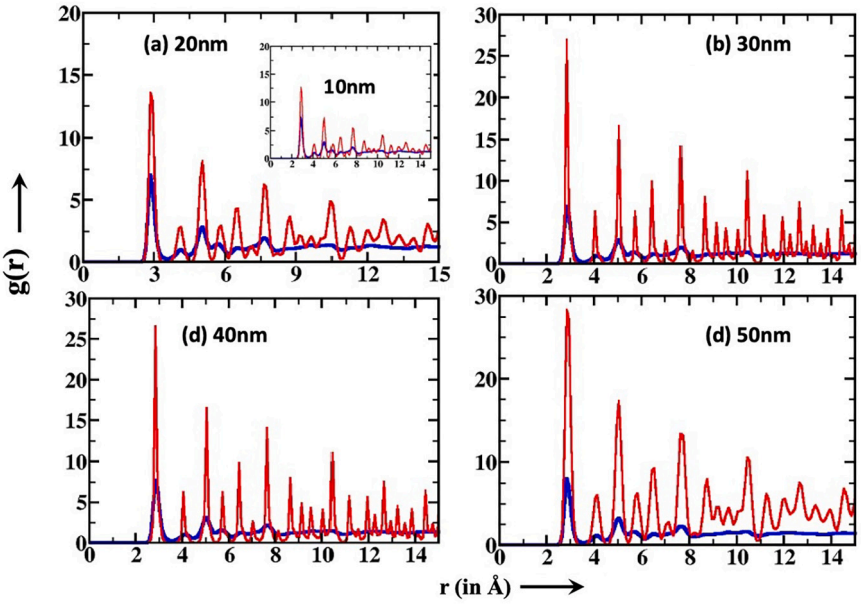

Fig. 4. Structural details of the Ag sintering before and after pulse application represented by radial distribution function (RDF). The red curves are pristine Ag RDF before pulse application. The blue curves are after pulse application and cooling the system to ambient temperature (27°C). The inset of (a) represents 10 nm NP sintering RDF before and after pulse application. The size of the nanoparticles is shown in legends.

The RDFs in Fig. 3(a), (b) show the distance of closest approach, $r_1 = 2.85$Å, the Goldschmidt diameter [40]. The Goldschmidt diameter is the distance of closest approach for a coordination number of 12 for FCC Ag crystal is, $r_1 = 2.86$Å, in excellent agreement with the simulated distance, $r_1 = 2.86$ Å, to within 0.35% of pristine Ag Goldschmidth distance. It is interesting to notice that the interatomic distance of Ag crystalline and liquid-like structures remain unchanged. This is because, elements crystallizing in close-packed structures, for example, FCC structures like copper and silver, the interatomic spacing do not change during solid-liquid phase transition.

After sintering, the Ag joined lines are cooled down to $300K$ to obtain the crystalline Ag wire at ambient temperature. The RDF for different size NP after sintering are shown in Fig. 3(c). For all the NP sizes, the FCC Ag peak positions can be observed at a shorter length-scales, until 10 Å. At longer length scales, hardly any structural features can be observed. The comparison of the RDFs before and after pulse sintering is shown in Fig. 4. As it can be observed for all the NP sizes, the peak heights after melting and cooling are smaller than the before sintering, i.e., the peak values are strongly attenuated for all the systems. The peak positions match until first 4 to 6 peaks. Beyond that crystalline structure of Ag disappears at longer length scale (> 10Å). Weaker peak height with no long-range structure is a characteristic of paracrystalline structure. Therefore, from these RDF observations, we can infer that the pristine FCC Ag crystal structure breaks down after sintering, and a paracrystalline structure of the sintered Ag line is evolved. The paracrystalline structure has been observed earlier by Jurkiewicz et al. [38] in metallic Ag nanoparticles. Paracrystallinity was first conceptualized by Laue [41], and subsequently theorized by Hosemann et al. [42,43]. However, paracrystalline structures in sintered Ag nanowires from Ag NP melting are observed for the first time in this work from atomistic structural details by performing large-scale atomistic MD simulation. Furthermore, paracrystalline structure cannot provide the pure FCC lattice that is needed for high conductivity of sintered Ag NPs and the reduction of conductivity in sintered Ag NPs are the consequences of lack of pure FCC crystallinity of Ag.

The paracrystalline structure of Ag line wires representing of pristine FCC structure can have immense impact on the fundamental properties of printed Ag lines. The percentage of FCC structure that is retained after sintering and cooling are tabulated in Table 1 derived from adaptive common neighbor analysis (CNA) calculations. For all size particles, between 31% to 34% FCC structures are retained, except for 100 nm Ag particle. A higher percentage of hexagonal closed pack (HCP) are observed between 20 nm to 50 nm particles. This may be due to the fact that the surface structures are not properly calculated as FCC in CNA calculations as the full 3D representation at the surface is not possible. The breakdown of FCC structures is observed in Fig. 3 and Fig. 4. We observed that a higher percentage of FCC structures in Ag lines printed from 30 nm particles.

Table 1
Percentage of different types of crystalline structures as obtained from common neighbor analysis using adaptive cutoff method.

NP size	% of FCC	% of HCP	% of BCC	% of Others
10 nm	31.8	19.3	6.1	42.7
20 nm	32.5	21.1	5.9	40.5
30 nm	34.0	22.2	5.7	38.1
40 nm	32.9	22.0	6.2	38.8
50 nm	33.1	22.4	6.2	38.3
100 nm	30.7	19.1	4.9	45.7

Finally, we performed a test simulation of sintering of two 100 nm Ag particles having more than 60.5 million atoms. To date, this is the largest simulation of sintering of two nanoparticles to our knowledge as it is computationally challenging to melt such a large number of atoms within a reasonable computational time frame. The radial distribution function of pristine 100 nm Ag NPs before, after pulse heating and cooled equilibrated structures are shown in Fig. 5a-c snapshots. In Fig. 5d, the RDF shows breakdown of pristine Ag structures before and after pulse heating. The liquid phases after melting are shown in Fig. 5e representing liquid-like RDF, and breakdown of FCC structures in Fig. 5f. In NP sintering, the joining process starts with a neck formation, then interfacial growth due to surface diffusion that allows grain-boundary diffusion [44]. Grain-boundary diffusion enhances the neck growth resulting in completely joined NPs forming smooth nanowires as seen in Fig. 1. However, for microparticles, in this case 100 nm, the grain-boundary diffusion becomes weaker resulting in two NPs fused together in a neck formation as seen in Fig. 5a-c that hinders smooth joint formation. This may also lead to lower conductivity in InkJet printed Ag nanowires for Ink with larger nanoparticles.

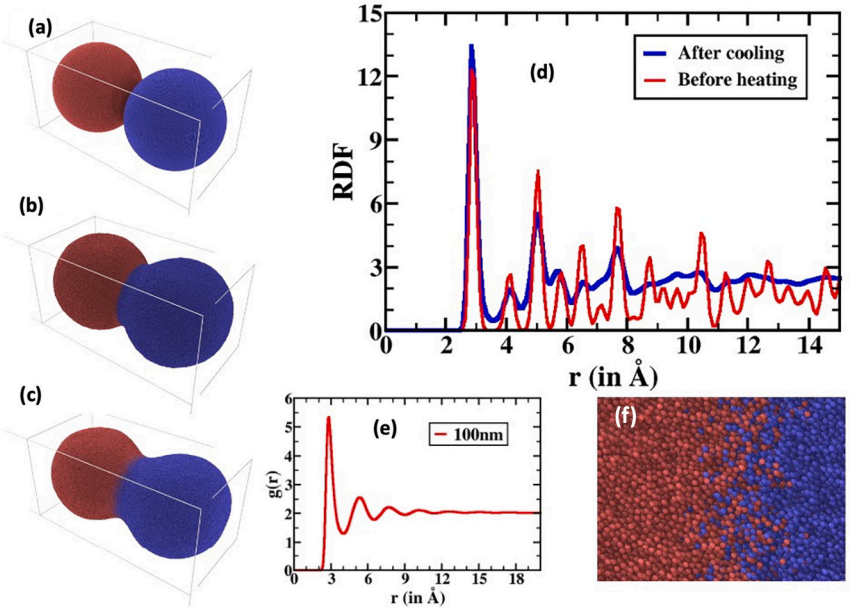

Fig. 5. Structural detail of 100 nm Ag nanoparticle sintering containing > 60.5 million atoms as represented by simulation snapshot and radial distribution functions (RDF). Snapshots of the sintering process before (a), after pulse heating (b), and cooling down to 27^{o}C after pulse applications (c). (d) Atomistic RDF before and after sintering and cooling. (e) Liquid phase RDF of the 100 nm Ag NP after sintering but before cooling showing liquid-like structure. (e) Snapshot of the interface in liquid phase (after pulse heating) showing no Ag FCC structure, red and blue spheres are from two different nanoparticles.

4. Conclusion

In this work, we performed large-scale atomistic simulations to understand the structural detail of Ag NP sintering for InkJet printed Ag nanowires. To our knowledge, these simulations are largest to date in understanding physics of sintering process of Ag nanoparticles generally found in Ag-Ink for printable electronics applications. From the analysis of simulation data, we conclude that pristine FCC structure of Ag crystal breaks down during sintering process. After cooling down the printed Ag lines, the lines lose the fundamental Ag FCC structure. This might be the key factor leading to drop of the conductivity during pulse thermal power (PTP) processing of Ag nanowires using InkJet printers [8]. We observed that intermediate size nanoparticles (30 nm) can give higher percentage of FCC structure, however, macroparticles (100 nm) forms neck between joined particles that can increase resistance and hence drop in conductivity. Therefore, we can conclude to a high degree that intermediate size NPs for Ag ink would be a better choice for extracting the full potential of highly conducting printed Ag nanowires. It must be noted that there are other important factors during PTP printed Ag wires that have not been taken into account in this study. The Ag Ink is colloidal dispersion of 20% Ag NPs in ethanol. We have not taken into account of the effect of Ag NP concentration in the Ink affecting the printed Ag lines properties. Secondly, we have not considered the effect of ethanol during printing. However, it should not be an important factor deciding the conductivity of the printed Ag lines because ethanol is completely evaporated during PTP process at high temperature (boiling point ethanol, 78.5^{o}C). Moreover, we have not taken into consideration different substrates or the roughness of the substrate and size distribution of the nanoparticles [45], that are essential to form a high performance electronic sensors. While these are important factors in deciding the final conductivity of the printed wires, this study focuses one of the many aspects, i.e., the crystal structure of sintered nanoparticles present in the Ink. We plan to include the these other important aspect in our future simulation and experimental works. We believe that this work will help design better Ag Ink for printed electronics applications.

Declaration of competing interest

The authors declare that they have no known competing financial interests or personal relationships that could have appeared to influence the work reported in this paper.

Data availability

The data that support the findings of this study are available from the corresponding author upon reasonable request.

Acknowledgements

This work was sponsored by the U.S. Department of Energy (DOE) Building Technologies Office (BTO) and Office of Electricity (OE) under contract number DE-AC05-00OR22725 with UT-Battelle LLC. MD simulations used resources of the Oak Ridge Leadership Computing Facility at the ORNL, which is supported by the Office of Science of the U.S. DOE under Contract No. DE-AC05-00OR22725. Part of the MD simulations used resources of the National Energy Research Scientific Computing Center (NERSC), a DOE Office of Scientific User Facility supported by the DOE Office of Science under Contract No. DE-AC02- 05CH11231.

References

[1] H.W. Tan, Y.Y.C. Choong, C.N. Kuo, H.Y. Low, C.K. Chua, 3d printed electronics: processes, materials and future trends, Prog. Mater. Sci. 127 (2022) 100945, https://doi.org/10.1016/j.pmatsci.2022.100945.

[2] G. Schmidt, H. Kempa, U. Fuegmann, T. Fischer, M. Bartzsch, T. Zillger, K. Preissler, U. Hahn, A. Huebler, Challenges and perspectives of printed electronics, in: Z. Bao, D.J. Gundlach (Eds.), Organic Field-Effect Transistors V, vol. 6336, SPIE, 2006, p. 633610.

[3] F. Wang, P. Mao, H. He, Dispensing of high concentraion ag nanoparticles ink for ultra-low resistivity paper-based writing electronics, Sci. Rep. 6 (2016) 21398.

[4] K. Cherenack, C. Zysset, T. Kinkeldei, N. Munzenrieder, G. Troster, Smart textile-integrated microelectronic systems for wearable applications, Adv. Mater. 32 (2020) 1901958, https://doi.org/10.1002/adma.201901958.

[5] E.S. Muckley, T. Aytug, R. Mayes, A.R. Lupini, J.-M.Y. Carrillo, M. Goswami, B.G. Sumpter, I.N. Ivanov, Hierarchical tio2:cu2o nanostructures for gas/vapor sensing and co2 sequestration, ACS Appl. Mater. Interfaces 11 (2019) 48466.

[6] M. Tatarko, E.S. Muckley, V. Subjakova, M. Goswami, B.G. Sumpter, T. Hianik, I.N. Ivanov, Machine learning enabled acoustic detection of sub-nanomolar concentration of trypsin and plasmin in solution, Sens. Actuators B, Chem. 272 (2018) 282.
[7] K. Cherenack, C. Zysset, T. Kinkeldei, N. Munzenrieder, G. Troster, Woven electronic fibers with sensing and display functions for smart textiles, Adv. Mater. 22 (2010) 5178, https://doi.org/10.1002/adma.201002159.
[8] P.C. Joshi, T. Kuruganti, S.M. Killough, Impact of pulse thermal processing on the properties of inkjet printed metal and flexible sensors, ECS J. Solid State Sci. Technol. 4 (2015) P3091.
[9] J.H. Noh, P.C. Joshi, T. Kuruganti, P.D. Rack, Pulse thermal processing for low thermal budget integration of igzo thin film transistors, IEEE J. Electron Devices Soc. 3 (2015) 297–301, https://doi.org/10.1109/JEDS.2014.2376411.
[10] Y. Yu, A.K. Mikkilineni, S.M. Killough, T. Kuruganti, P.C. Joshi, A. Hu, Direct-write printed current sensor for load monitoring applications, in: 2019 IEEE Power & Energy Society Innovative Smart Grid Technologies Conference (ISGT), 2019, pp. 1–6.
[11] Y. Yu, M. Chen, S. Wang, C. Hill, P.C. Joshi, T. Kuruganti, A. Hu, Laser sintering of printed anodes for al-air batteries, J. Electrochem. Soc. 165 (2018) A584.
[12] P.C. Joshi, S.M. Killough, P.T. Kuruganti, Wireless sensor platform, https://patents.google.com/patent/US9729193B2/en, 2014, US, Patent 9,729,193.
[13] K. Black, J. Singh, D. Mehta, S. Sung, C.J. Sutcliffe, P.R. Chalker, Silver ink formulations for sinter-free printing of conductive films, Sci. Rep. 6 (2016) 20814.
[14] S.K. Volkman, S. Yin, T. Bakhishev, K. Puntambekar, V. Subramanian, Mechanistic studies on sintering of silver nanoparticles, Chem. Mater. 23 (2011) 4634.
[15] J. Nittynen, E. Sowade, H. Kang, R.R. Baumann, M. Mantysalo, Comparison of laser and intense pulsed light sintering for inkjet-printed copper nanoparticle layers, Sci. Rep. 5 (2015) 8832.
[16] Y. Tang, W. He, S. Wang, Z. Tao, L. Cheng, New insight into the size-controlled synthesis of silver nanoparticles and its superiority in room temperature sintering, CrystEngComm 16 (2014) 4431.
[17] M. Grouchko, A. Kamyshny, C.F. Mihailescu, D.F. Anghel, S. Magdassi, Conductive inks with a “built-in” mechanism that enables sintering at room temperature, ACS Nano 5 (2011) 3354–3359.
[18] J. Park, J. Sharma, M. Goswami, D. Voylov, G.G. Jang, M.G. Lassiter, A. Marquez-Rossy, G. Polizos, Solution derived monolithic thin films with low adhesion energy, Sol. Energy Mater. Sol. Cells 206 (2020) 110302.
[19] D. Xiang, X. Wang, C. Jia, T. Lee, X. Guo, Molecular-scale electronics: from concept to function, Chem. Rev. 116 (2016) 4318–4440.
[20] A. Vezzoli, Metal Complexes and Clusters in Single-Molecule Electronics, John Wiley & Sons, Ltd, 2021, pp. 1–21.
[21] J. Chen, A.M. Rawlett, J.M. Large, Large on-off ratios and negative differential resistance in molecular electronic device, Science 286 (1999) 1550.
[22] J. Ponce, C.R. Arroyo, S. Tatay, R. Frisenda, P. Gavina, D. Aravena, E. Ruiz, H.S.J. van-der Zant, E. Coronado, Effect of metal complexation on the conductance of single-molecular wires measured at room temperature, J. Am. Chem. Soc. 136 (2014) 8314.
[23] R. Wu, X. Zhao, Y. Liu, Atomic insights of cu nanoparticles melting and sintering behavior in cu-cu direct bonding, Mater. Des. 197 (2021) 109240.
[24] A. Abedini, A. Malti, A. Kardani, A. Montazeri, Probing neck growth mechanism and tensile properties of sintered multi-nanoparticle al-cu systems via md simulations, Adv. Powder Technol. 34 (2023) 104084.
[25] M.S. Daw, M.I. Baskes, Semiempirical quantum mechanical calcuation of hydrogen embrittlement in metals, Phys. Rev. Lett. 50 (1983) 1285.
[26] S.M. Foiles, M.I. Baskes, M.S. Daw, Embedded-atom-method functions for the fcc metals cu, ag, au, ni, pd, pt and their alloys, Phys. Rev. B 33 (1986) 7983.
[27] A.P. Thompson, H.M. Aktulga, R. Berger, D.S. Bolintineanu, W.M. Brow, P.S. Crozier, P.J. Veld, A. Kohlmeyer, S.G. Moore, T.D. Nguyen, R. Shan, M.J. Stevens, J. Tranchida, C. Trott, S.J. Plimpton, Lammps - a flexible simulation tool for particle-based materials modeling at the atomic, meso and continuum scale, Comput. Phys. Commun. 271 (2022) 108171.
[28] A. Stukowski, Visualization and analysis of atomistic simulation data with ovito - the open visualization tool, Model. Simul. Mater. Sci. Eng. 18 (2010) 015012.
[29] B. Li, X. Wen, R. Li, Z. Wang, P.G. Clem, H. Fan, Stress-induced phase transformation and optical coupling of silver nanoparticle superlattices into mechanically stable nanowires, Nat. Commun. 5 (2014) 4179.
[30] M. Goswami, N. Kumar, Y. Li, J. Hirschey, T.J. LaClair, D.O. Akamo, S. Sultan, O. Rios, K.R. Glusenkamp, S. Graham, Understanding supercooling mechanism in sodium sulfate decahydrate phase-change material, J. Appl. Phys. 129 (2021) 245109.
[31] M. Lin, G. Gottstein, L. Shvindlerman, Generalized gibbs-thomson equation for nanoparticles at grain boundaries, Acta Mater. 129 (2017) 361.
[32] P. Peng, A. Hu, A.P. Gerlich, G. Zou, L. Liu, N. Zhou, Joining of silver nanomaterials at low temperatures: processes, properties, and applications, ACS Appl. Mater. Interfaces 7 (2015) 12597.
[33] K. Lu, Sintering of nanoceramics, Int. Mater. Rev. 53 (2008) 21.
[34] Z. Fang, H. Wang, Densification and grain growth during sintering of nanosized particles, Int. Mater. Rev. 53 (2008) 326.
[35] Y. Zhu, J. Lian, Q. Jiang, Modeling of the melting point, debye temperature, thermal expansion coefficient, and the specific heat of nanostructured materials, J. Phys. Chem. C 113 (2009) 16896.
[36] A. Chernyshev, Effect of nanoparticle size on the onset of surface melting, Mater. Lett. 63 (2009) 1525.
[37] G. Ouyang, T. X, G. Yang, Thermodynamic model of the surface energy of nanocrystals, Phys. Rev. B 74 (2006) 195408.
[38] K. Jurkiewicz, M. Kaminski, W. Glajcar, N. Woznica, F. Julienne, P. Bartczak, J. Polanski, J. Lelatko, M. Zubko, A. Burian, Paracrystalline structure of gold, silver, palladium and platinum nanoparticles, J. Appl. Crystallogr. 51 (2018) 411.
[39] C.N.J. Wagner, H. Ocken, M.L. Joshi, Interference and radial distribution functions of liquid copper, silver, tin, and mercury, Z. Naturforsch. Teil A 20 (1965) 325–335.
[40] W. Hume-Rothery, Structure of Metals and Alloys, Institute of Metals, London, 1945.
[41] M. von Laue, Rontgenstrahl-Interferenzen, 3rd ed., Akademie Verlagsges, Frankfurt, 1960, ch. 3.
[42] R. Hosemann, S.N. Bagchi, Direct Analysis of Diffraction by Matter, North Holland, Amsterdam, 1960.
[43] A.M. Hindeleh, R. Hosemann, Microparacrystals: the intermediate stage between crystalline and amorphous, J. Mater. Sci. 26 (1991) 5127.
[44] L. Ding, R.L. Davidchack, J. Pan, A molecular dynamics study of sintering between nanoparticles, Comput. Mater. Sci. 45 (2009) 247.
[45] G. Yang, H. Lai, W. Lin, J. Tong, J. Cao, J. Luo, Y. Zhang, C. Cui, A quantitative model to understand the microflow-controlled sintering mechanism of metal particles at nanometer to micron scale, Nanotechnology 32 (2021) 505721.